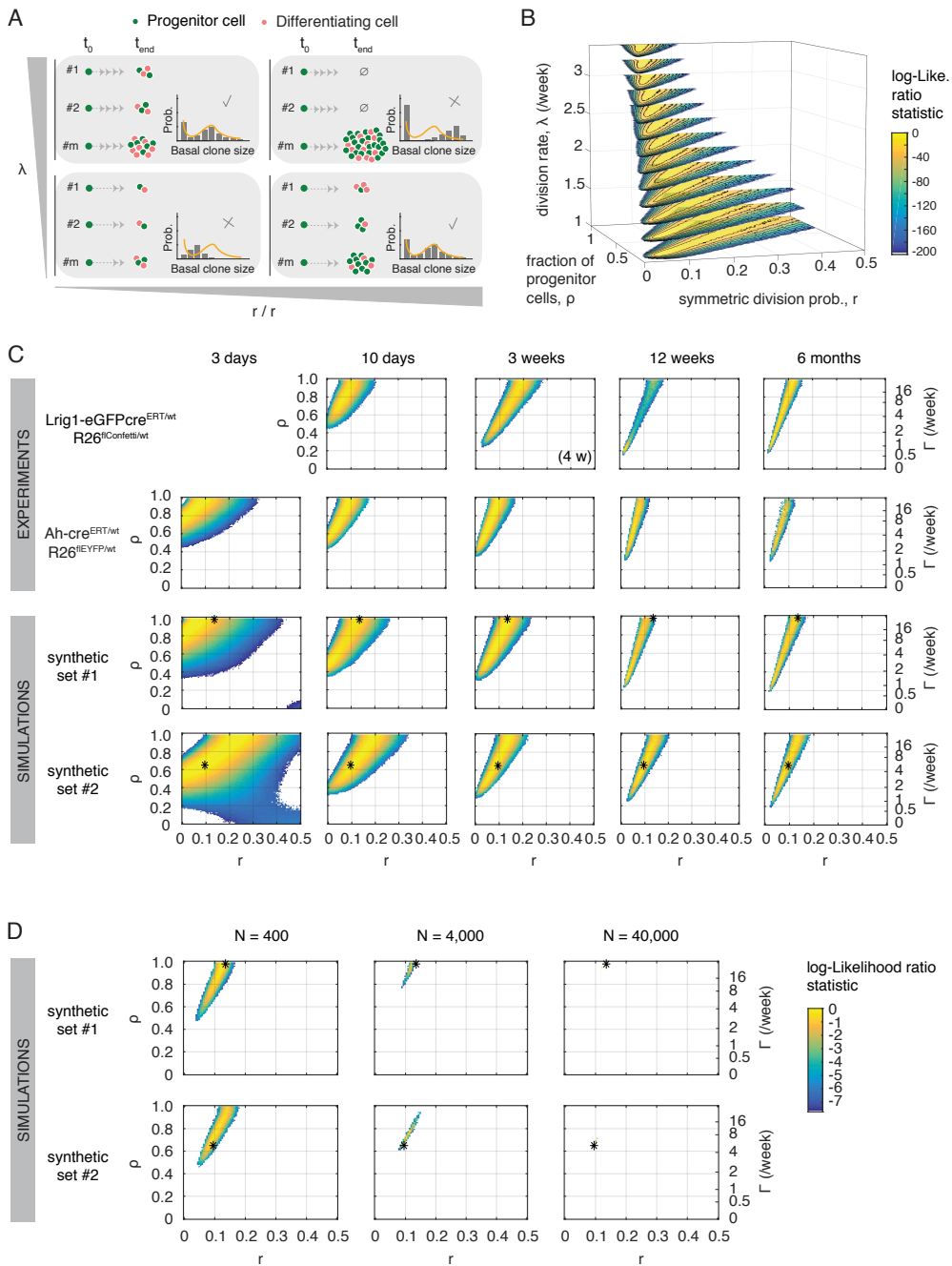


Supplementary Figures, Legends and Methods (Supplementary references at the end of this file)

Supplementary Figure 1



Supplementary Figure 1 Challenges in single progenitor model parameter inference. (A-B) Uncertainty over the progenitor-cell division rate λ can affect the accuracy of inferring the value of the other model parameters (r , ρ) (see **Figure 6**). (A) Scheme illustrating the possible fate of different simulated clones (#1, #2, #m) under various parameter scenarios. For low ratios of r/ρ most divisions are predicted to be asymmetric, but a high value of λ results in a broadens the clone size distributions at a given time point t_{end} (grey bars). Similar effects could be expected if λ remained unchanged but r/ρ ratio increased, since this results in a higher probability of symmetric division events. Thus, different parameter values could provide adequate fits to an experimental clone size distribution (depicted as orange lines). (B) MLE inference of the SP model parameters from experimental basal clone sizes. Data from lineage tracing in *Lrig1-eGFPcre^{ERT/WT} R26^{flConfetti/WT}* mice esophagus are taken for illustration. 3D parameter solutions are color-coded according to likelihood value (fittings worsen as the log-likelihood ratio statistic gets more negative; values < -200 are not displayed). Without prior knowledge on cell proliferation rates, it is hard to resolve the dynamics, with semi-optimal solutions (yellow regions) spread across multiple values of λ . (C-D) Sample size and timing influence parameter estimates. (C) 2D heat maps showing most likely parameter values obtained when analyzing, under the SP paradigm – with prior knowledge on λ – and for each time point separately, experimental *Lrig1*- and *Ah-Cre^{ERT}* derived clonal data from esophagus and, in parallel, synthetic clonal data simulated under specific parameter conditions (shown in asterisks) and subjected to reanalysis. In all cases, 100 randomly-chosen clones were analyzed per data set per time to correct for possible biases due to differences in sample size. Results are averages from bootstrapping. (D) SP model parameter discrimination improves as increasing the sample size. The same synthetic data sets described above were used, and inference analyses repeated by randomly sampling 100, 1,000 and 10,000 clones per time point at four time points (1, 2, 4, and 6 weeks), i.e. a total of $N = 400, 4,000$ and $40,000$ clones. Results are shown as bootstrapping averages.

A

Markovian vs. Non-Markovian

Time

Basal clone size

Progenitor cell (green dot), Differentiating cell (red dot), Suprabasal cell (pink dot)

$t_{cc} \sim \text{Exp}(\lambda)$

$t_{cc} \sim t_R + \text{Gam}(k, q)$

B

KL Divergence (clone size distributions)

Time (days)

T_c

lag time, t_{ln} (days)

GAM-distribution shape (k)

$\langle T \rangle$ (weeks)

GAM t_{cc} (red), EXP t_{cc} (grey)

C

Basal clone size

0.5 week, 1 week, 2 weeks, 4 weeks

D

3 days, 1 week, 2 weeks, 4 weeks, overall

synthetic set #3, synthetic set #4

ρ , r , Γ (week)

E

10 days, 3 weeks, 12 weeks, 6 months

Lig1-eGFP^{ERT/Net}, R26^{Cre/Confetti/Net}, Ah-cre^{ERT/Net}, R26^{YFP/Net}

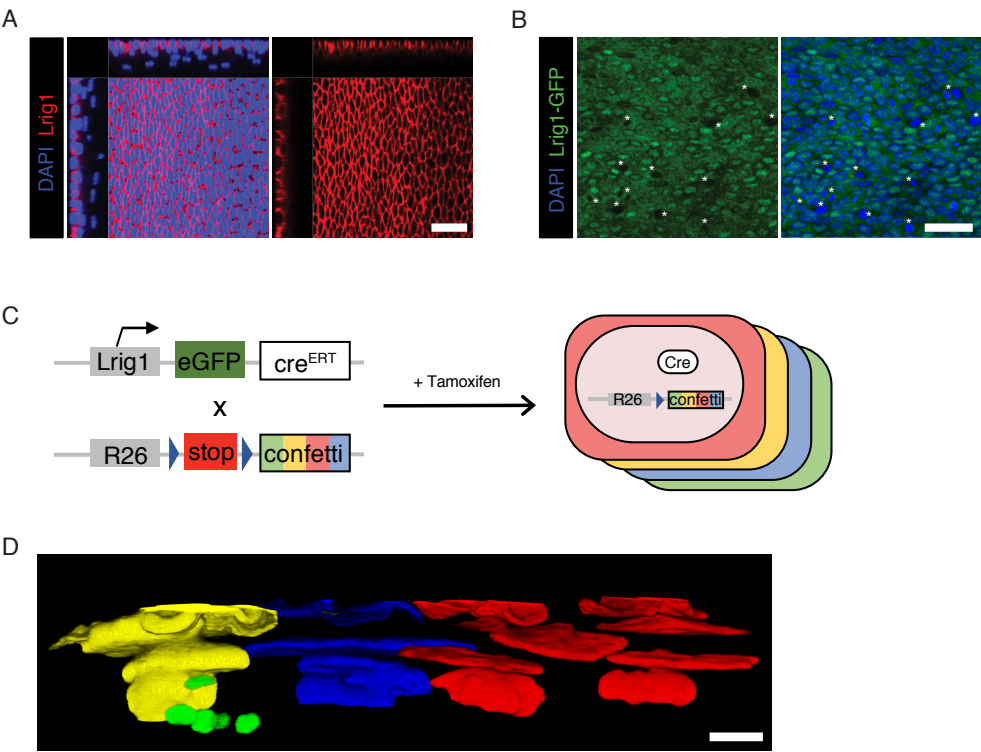
ρ , r , Γ (week)

log-Likelihood ratio statistic

EXP t_{cc} , GAM t_{cc}

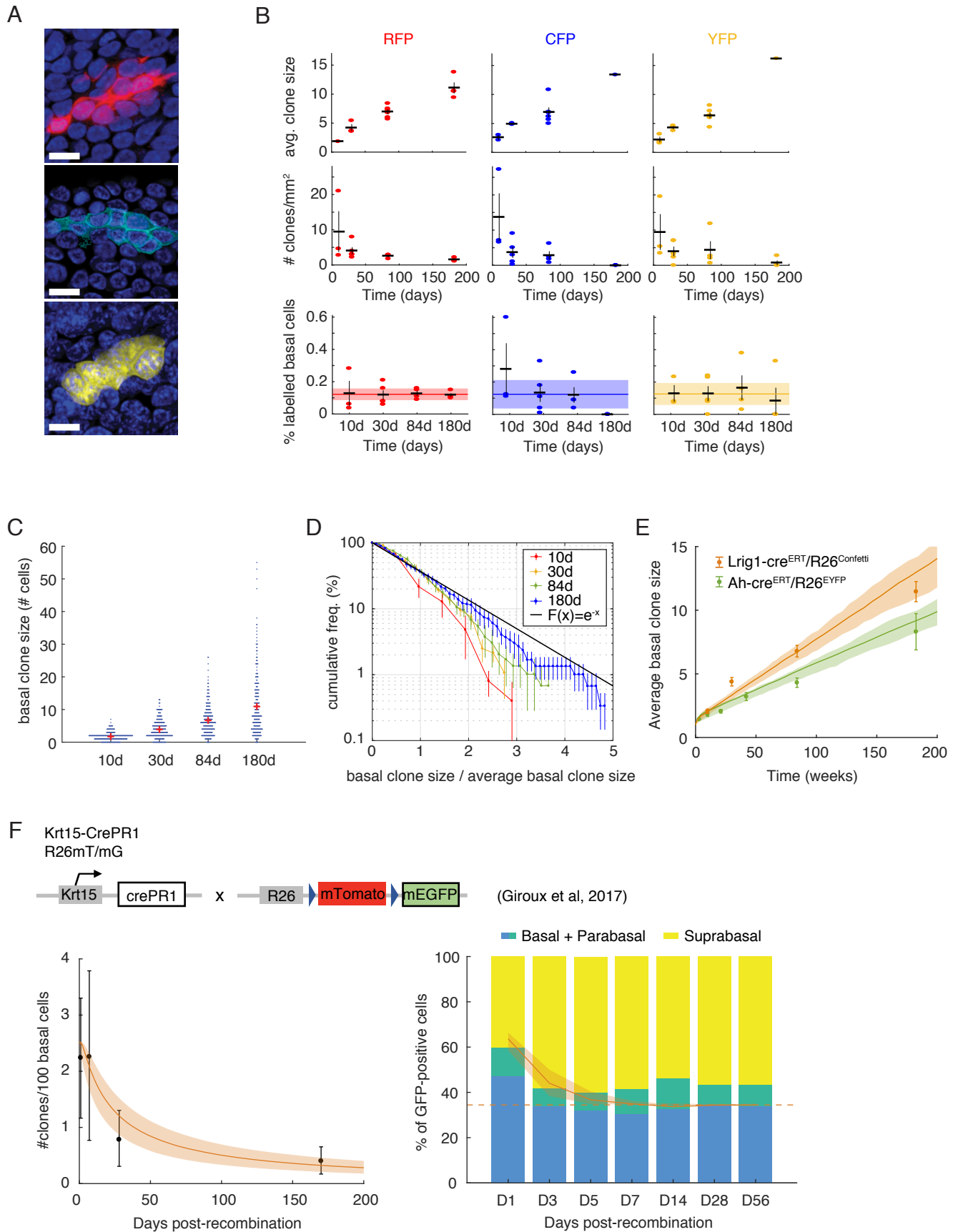
Supplementary Figure 2 The cell-cycle time distribution impacts parameter inference from clone size distributions. (A) Schematic illustration of clonal dynamics inferred for the SP model under two different cell cycle time (t_{cc}) distributions of the individual cell-cycle time: exponential (*EXP*) and a delayed gamma distribution (*GAM*), where cells can only divide after a minimum refractory period τ_R (with shape controlled by parameter κ). Despite the distributions sharing the same average cell-cycle time (blue vertical line), the broad *EXP* distribution predicts that individual clones (#1, #2, #3, #m) will have a wider distribution of sizes (grey bars) after a short time chase (t_1) than the *GAM* distribution. This difference is less apparent after multiple rounds of division (t_2). Thus, the form of the cycle time distribution can impact parameter inference of experimental clone sizes (orange lines) at early time points after cell labelling. (B) Time evolution of the Kullback-Leibler (KL) divergence between basal clone-size frequencies obtained from a limited set of simulated clones (300 clones per time point) following an exponential (grey) or gamma (red; $\tau_R=0.5$ days, $\kappa=8$) t_{cc} , and the theoretical clone-size distribution predicted for an idealized infinite population under the exponential t_{cc} paradigm (lower values indicate a closer match). Solid lines and shaded regions stand for the average and 95% confidence intervals respectively on KL values from 100 independent sets. The average critical time T_c (dashed line) after which clone-size distributions from gamma and exponential t_{cc} assumptions converge is reported as a heat map for various shapes of the cell-cycle distribution (all simulations carried out with $\lambda=2.9/\text{week}$, $\rho=0.65$, $r=0.1$). (C) Detail of differences in simulated basal clone-size distributions obtained at early time points under an exponential- (grey) vs. gamma- (red) distributed t_{cc} (parameter values as above). Data shown as average \pm 95% CI on frequencies, $n = 100$ independent simulations. (D) Parameter inference obtained at different time points from simulated clone-size datasets (1,000 clones per time point) run under the paradigm of a gamma-distributed t_{cc} ($\tau_R=0.5$ days, $\kappa=8$). In red scale: accepted parameter values when considering the actual t_{cc} distribution as a given prior. In grey scale are results assuming a default exponential t_{cc} distribution. Results are averages from bootstrapping. Neglecting the details of the cell-cycle period distribution can lead to deviations from the true parameter values (in asterisks). Similarly, parameter estimates obtained from *Lrig1*- and *Ah-Cre^{ERT1}* derived experimental data sets in esophagus (100 clones per time point) do vary depending on the t_{cc} assumptions used in the inference analysis (E).

Supplementary Figure 3



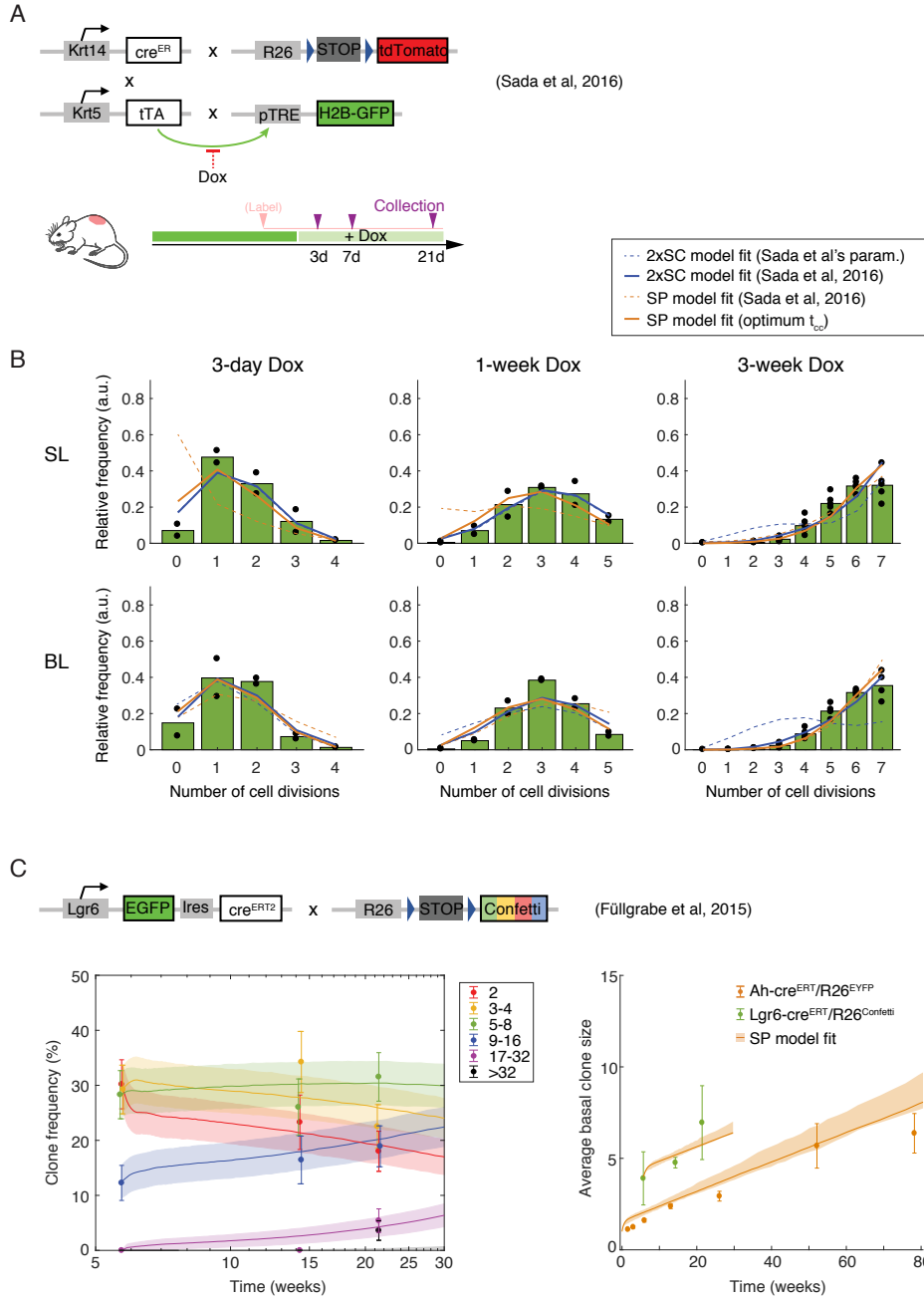
Supplementary Figure 3 Experimental model used for lineage tracing in esophageal epithelium. (A) xyz plane views of confocal images showing *Lrig1* expression in wild type mice confined to the basal layer of the esophageal epithelium, where it is widespread. Red: LRIG1 immunostaining; blue: DAPI. Scale bar, 40 μ m. Images are representative of 9 fields of view in 3 individual biologically independent mice (B) Rendered confocal z stacks of the basal layer in *Lrig1-eGFP-cre^{ERT}* mice showing *Lrig1*-driven GFP expression (green); blue: DAPI. *Lrig1*-GFP negative cells correspond with bright, condensed, mitotic nuclei (asterisks). Scale bar, 40 μ m. (C) Description of the transgenic mouse model used for lineage tracing. An *eGFP-IRES cre^{ERT2}* construct was inserted in the exon 1 of the endogenous *Lrig1* locus, and a conditional confetti expression construct containing a “stop” cassette flanked by *LoxP* sites was targeted to the ubiquitous Rosa26 promoter. Upon induction with tamoxifen, Cre^{ERT} protein can migrate to the nuclei and excise the stop codon, resulting in the expression of one of the four different fluorescent proteins coded by confetti: GFP, YFP, RFP or CFP. Labelled, recombinant cells and their progeny (i.e. clones) can then be analyzed at different times. (D) 3D reconstruction of a confocal z stacks showing the side-view of an esophageal wholemount 30 days after induction in *Lrig1-eGFPcre^{ERT/wt} R26^{flConfetti/wt}* animals. Scale bar, 10 μ m.

Supplementary Figure 4



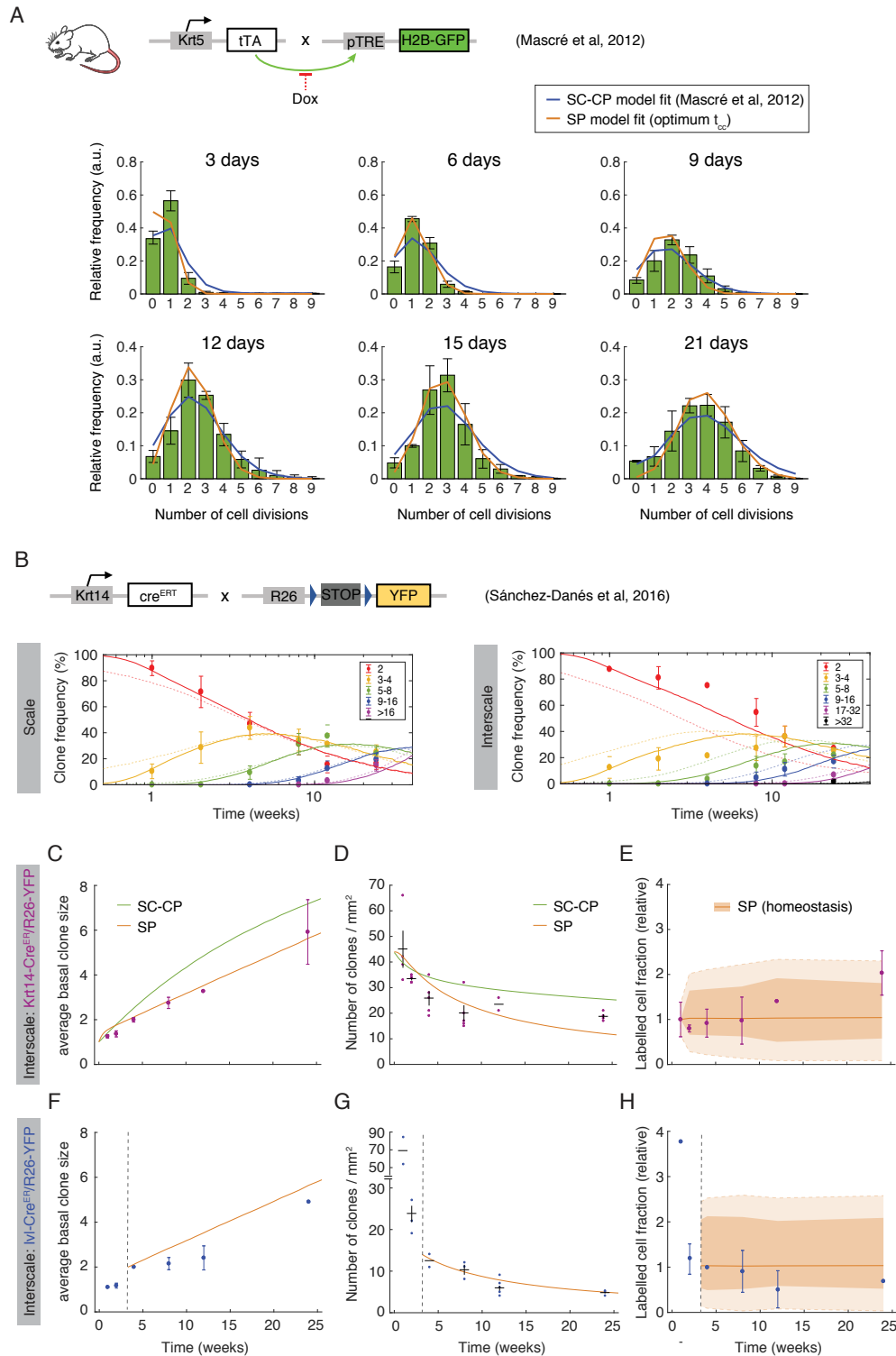
Supplementary Figure 4 Labelled clone dynamics in *Lrig1-cre^{ERT}/R26^{Confetti}* mouse esophagus and comparison to other lineage-tracing data sets. (A) Rendered confocal z stacks of the esophageal basal layer showing typical Confetti clones at 84 days post-induction. Red is RFP, light blue is CFP, yellow is YFP, blue is DAPI. Scale bars, 10 μ m. (B) Quantitative characteristics of RFP-, CFP-, and YFP- labelled clone populations over time: mean basal cells per clone (top panels), average density of labelled clones in the basal layer (middle panels), average fraction of labelled basal cells (bottom panels) at the indicated time points. Observed values (dots) and error bars (mean \pm s.e.m.) from $n \geq 3$ animals. Straight colored lines and shading in bottom panels indicate mean and s.e.m. across all time points, consistent with homeostatic behavior (note at latest time point CFP clones were not detected in the cohort of mice used for clone density and % labelled basal cell quantifications, probably due to low initial labelling efficiency and limited sampling). (C) Beeswarm plot showing *Lrig1* basal-layer clone sizes (number of basal cells/clone) over time in the esophageal epithelium. Red marks show average size at each time. Only *surviving* clones, containing at least 1 basal cell, were considered. (D) Histogram of cumulative clone size frequencies normalized to the average basal clone size at each time (dots with error bars: mean \pm s.e.m. from $n=3$ mice). At long term, distributions converge into a scaling behavior, where the probability of seeing clones of sizes larger than x times the average becomes constant and follows an exponential $F(x) = e^{-x}$. (E) Time evolution of the average basal-layer size of surviving clones in induced *Ah-cre^{ERT} R26^{EYFP}* mice ¹ as compared to *Lrig1-eGFP-cre^{ERT} R26^{flConfetti}*. Experimental data shown as dots with error bars (mean \pm s.e.m. from $n \geq 3$ animals). SP model fits shown in green and orange, respectively (solid lines stand for the MLE; light areas: 95% CI). (F) The inferred keratinocyte cell behavior from the *Lrig1-eGFP-cre^{ERT} R26^{flConfetti}* mice fits independent experimental lineage-tracing data from *Krt15-cre^{PR1} R26^{mT/mG}* mouse esophagus ², reproducing the decay in the basal clone density over time (left panel, dots indicate mean and error bars s.d) and the change in the proportion of labelled cells located in basal and suprabasal compartments (right panel). Experimental sets are from Fig. S3 and Fig. 2 in ², respectively. Model fits shown in orange (solid lines: MLE; light areas: 95% CI; dashed line corresponds with the estimated fraction of basal cells in homeostasis). See **Supplementary Data 4** for goodness of fit statistics.

Supplementary Figure 5



Supplementary Figure 5 The single-progenitor model fits independent transgenic-mouse data sets on keratinocyte behavior in dorsal skin. (A) Transgenic mouse model used by ³ to study epidermal cell proliferation in dorsal skin. Unlike *R26^{M2rtTA}/TetO-H2BGFP* mice (Tet-On), *Krt5^{rtTA}/pTRE-H2BGFP* mice show constitutive H2BGFP expression, and treatment with Dox is required for repression of H2BGFP production during the duration of the dilution experiment (Tet-Off; see Supplementary Figure 1). (B) Reanalysis of H2BGFP dilution data in ³. Distributions of cell division number after different chase periods, as deconvoluted from H2BGFP fluorescence histograms of FACS sorted basal and suprabasal (spinous-layer) cells (green bars; dots: individual-mice data). Data extracted from Figure 3 in ³. Our computational-simulation fits using a SP model with gamma-distributed cell-cycle times (solid orange lines) mimic the best fits provided by ³ using a 2xSC model (solid blue lines), while the latter results in deviated fits with the parameters claimed in their text (dashed blue lines). Poor SP-model fits from ³ (dashed orange lines) were due to oversimplified exponential cell-cycle assumptions. (C) The inferred keratinocyte cell behavior from *AhYFP* mouse back skin epidermis fits independent experimental lineage-tracing data from *Lgr6-eGFPcre^{ERT} R26^{flConfetti}* mice ⁴. Left panel: Empirical long-term, basal-layer clone size distributions are displayed as mean frequency \pm standard error of proportion (dots with error bars) for each clone size or basal cell number (in different colors). Lines and shaded areas correspond to the SP-model MLE predictions and ranges within \pm s.d. from bootstrapping (random sampling of experimental clone sizes at P8w were considered as starting condition for simulations on the *Lgr6*-based system, to account for the fact that induction occurred early in development, before mouse epithelia become homeostatic). Right panel: Time evolution of the average basal-layer size of surviving clones in *Lgr6-eGFPcre^{ERT} R26^{flConfetti}* mice (from ⁴) as compared to *Ah-cre^{ERT} R26^{EYFP}* mice ⁵. Experimental data shown as dots with error bars (mean \pm s.e.m. from $n \geq 3$ animals). SP model fits shown in orange (solid lines stand for the MLE; light areas: 95% CI), matching both average trends from single-labelled progenitors in the *Ah*-based data set and preformed clones in the *Lgr6*-based system. See **Supplementary Data 4** for goodness of fit statistics.

Supplementary Figure 6



Supplementary Figure 6 The single-progenitor model fits different transgenic-mouse data sets of keratinocyte behavior in tail skin. (A) Reanalysis of H2BGFP dilution data from $Krt5^{tTA}/pTRE-H2BGFP$

(Tet-Off; see **Figure 2**) mouse tail skin ⁶. Distributions of cell division number after different chase periods, as deconvoluted from H2BGFP fluorescence histograms of FACS sorted basal cells (green bars with error bars: mean \pm s.e.m. from $n = 3$ individual animals). Data extracted from Fig. 3 in ⁶. Our computational simulations using a SP model with gamma-distributed cell-cycle times (solid orange lines) show as good a fit to the data as the more complex SC-CP model used by ⁶ (solid blue lines). Unrealistic, exponential cell-cycle time distributions were considered in the original publication. (B) Basal clone size distributions in scale and interscale regions of tail following lineage tracing in *Krt14-cre^{ERT} R26^{YFP}* mice ⁷. Frequencies for each clone size are in different colors (dots with error bars: empirical values reported, along with standard error of the proportion). Solid lines: SP-model MLE fits obtained using as a prior the value for the average division rate measured by ⁶ and a reasonable gamma-shaped cell-cycle time distribution. Dim dashed lines: fits obtained using the parameterized models described in ⁷, where a SC-CP scenario is considered in interscale. (C, D, F, G) Time course of the average basal-layer size and density of clones labelled with *Cre^{ERT}* expressed from *Krt14* or *Ivl* promoters in interscale (purple and blue datasets, respectively; dots indicate mean and error bars s.e.m for time points $n > 2$ mice) ⁷. Numbers of biologically independent mice are (C,D $n = 4, 3, 5, 5, 2, 4$ mice and F,G $n = 2, 3, 2, 3, 5, 2$ mice at 1,2, 4, 8,12, and 24 weeks respectively. Orange lines: fits obtained with the SP model with same parameter values determined from (B). Green lines: fits on *Krt14*-derived data obtained from the parameterized SC-CP model used by ⁷. (E, H) Changes in the labelled cell fraction derived for both *Krt14-cre^{ERT} R26^{YFP}* (E) and *Ivl-cre^{ERT} R26^{YFP}* (H) experimental model data sets (error bars: mean \pm s.d.) (inferred by multiplying average labelled clone densities by average clone sizes at each time, accounting for error propagation). Possible experimental trends fall within the domain of uncertainty given by the SP model in homeostasis considering the large errors due to the actual limited sample size (dark orange area: 95% CI on the mean; light orange area: margins given with \pm s.d.) (see Supplementary Theory for details). See **Supplementary Data 4** for goodness of fit statistics.

Supplementary Methods (Supplementary references at the end of this file)

This report is intended to provide a detailed description of the methodology used in the Main Text and the quantitative arguments supporting the paradigm of a single population of progenitor cells in squamous epithelia. In **section 1** we describe some control measures to test the adequacy of our experimental system for lineage tracing in esophagus. In **section 2** we formulate the different stochastic models of cell behavior and discuss the limitations that clonal dynamics features present for model discrimination. In **section 3** we describe the methods used to infer a single mode of keratinocyte cell proliferation. **Section 4** follows with the combined approach used for model inference on clonal lineage-tracing data sets constrained by cell-cycle properties. Finally, in **section 5** we revisit the quantitative methodology and arguments from previous publications.

1. Lineage-tracing controls and labelling representativeness

In the main text, we describe a lineage tracing experiment in esophageal epithelium using inducible *Lrig1-eGFPcre^{ERT} R26^{flConfetti}* mice. Before introducing the quantitative methods and theory involved in clonal fate analysis, in this section we address some controls regarding the labelling representativeness of self-renewal in this tissue.

Lrig1 was ubiquitously expressed throughout the basal layer of the esophageal epithelium, where proliferation is confined (see immunostaining; **Supplementary Figure 3A**), and *Lrig1*-driven GFP expression reporting *Lrig1* transcription was detectable in more than 94% of the basal cells (**Supplementary Figure 3B**). This argues that *Lrig1*-derived labelled clones widely represent basal keratinocyte dynamics in the esophageal epithelium.

An inducible *Cre/Confetti* reporter was used to track the fate of *Lrig1*-expressing basal cells (**Supplementary Figure 3C**). To exclude the possibility of spontaneous fluorescence reporter expression, esophageal epithelia were collected from uninduced, 12-16 week old mice ($n=3$), confirming the absence of any labelled clone and hence of any leakage (**Supplementary Data 5**). Following low-dose tamoxifen administration, CFP-, RFP- and YFP-labelled cell patches were analyzed for clonal behavior at different times post-induction. The low total labelling efficiency (1 in 301 ± 106 (mean \pm SEM) basal cells by 10 days post induction; **Supplementary Data 5**) and distinction of different fluorescent colors minimizes the risk of clonal merging⁸, so that single-color patches were considered clonal. Induced GFP-labelled cells were excluded from the analysis given the expression of GFP from the *Lrig1* locus.

The number of basal cells per clone, n (basal clone size), was counted, and the frequency of clones of a certain size x_n reported for each individual label reporter and time (**Supplementary Figure 4A-B; Supplementary Data 5**). No statistical differences in the distributions of clone size frequencies were seen between CFP, RFP and YFP labelled cell populations at any given

time (Kruskal-Wallis test, $p = 0.17, 0.27, 0.99, 0.22$ at time 10d, 30d, 84d, 180d, respectively; non-significant too by pairwise comparisons using Kolmogorov-Smirnov test), justifying pooling the data from the different label reporters (**Figure 7**). In the case where the time courses in the number of clones per unit area and the proportion of labelled basal cells were shown, only RFP clones were considered, given the low, variable induction of the other fluorescent reporters (including these numbers did not alter the conclusions).

Importantly, overall, the fraction of Confetti labelled basal cells remained approximately constant over time (**Figure 7C**). This agrees with homeostatic behavior and strongly supports the hypothesis that the labelled cell population is representative of the epithelial self-renewal.

2. The possible models of epithelial cell dynamics

Homeostasis is a fundamental feature of adult tissues. Whilst the specific mechanisms for homeostasis may vary depending on the organization of the niche itself, within squamous epithelia several models have been proposed that are sufficient to explain tissue maintenance. These can be broadly separated based on two key features: the presence of a single or multiple dividing population, and whether the progeny fates are balanced by a deterministic or stochastic process. Deterministic processes (*invariant asymmetric self-renewal*) lead to the growth of stable, similar sized clones over long periods of time following labelling of stem cells, regardless of the presence or absence of transient amplifying cells (cells that have a limited division capacity)⁹. In contrast, stochastic models (*population asymmetric self-renewal*) achieve balance by allowing individual cells to divide either asymmetrically or symmetrically, with an equal probability of symmetric stem or differentiation fates (**Figure 1D**). A consequence of these branching processes is that clones exist in neutral competition, and develop heterogeneous sizes over time as some grow, whilst others diminish or even become extinct. Here we briefly review this latter class of models and the evidence that supports them.

Several features of the clone size distributions arise from population asymmetric self-renewal^{8, 10}:

- The number of surviving labelled clones, containing at least one basal cell, continuously decays over time, following a hyperbolic function, $P_{surv}(t) \sim 1/t$. This reflects the non-null probability of clone extinction.
- The average number of basal cells in the surviving clones grows linearly with time, $\langle n \rangle_{surv}(t) \sim t$, to compensate the decline in clone density, so that the overall cell population remains constant.
- The surviving clones display increasingly heterogeneous sizes. The distribution of basal clone sizes adopts a scaling behavior at long term, so that the chance of finding a

clone larger than some multiple of the average (a cumulative probability $P_{n > \langle n \rangle_{surv}(t)}^{cum}$ becomes constant, i.e. $P_n^{cum}(t) = f[n / \langle n(t) \rangle_{surv}]$, where, typically, $f(x) = e^{-x}$.

We found that these hallmarks are all fulfilled by the *Lrig1-eGFPcre^{ERT} R26^{flConfetti}* clonal data (**Figure 7; Supplementary Figure 4 C,D**), and also shared by lineage-tracing datasets across different skin territories (**Figure 8**), confirming self-renewal dynamics in mouse squamous epithelia is dominated by stochastic cell fates comprising both symmetric and asymmetric division outcomes.

However, it remains contested whether this stochastic clone dynamics is underpinned by a single population of dividing cells ¹⁰ or multiple populations. In different studies these multiple populations have been proposed either to coexist independently within a tissue ³ or with a hierarchical relationship between them ⁶ (**Figure 1D**). In the following subsections we formally describe the different models and explain their specific characteristics.

The single-progenitor model

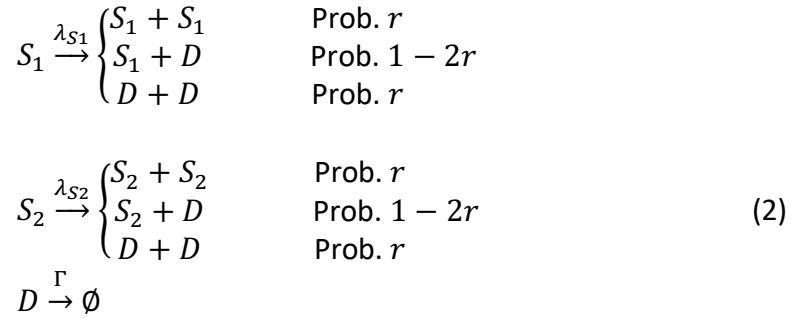
In the *single-progenitor model*, there is a single population of progenitor cells (P cells), which divide regularly, with an average rate λ , to give rise, with a certain probability, to either two daughter progenitors (P + P), two differentiating cells (D + D) or one of each (P + D) ¹⁰ (**Figure 1D**). Differentiating cells (D) are post-mitotic and leave the basal layer with stratification rate Γ , constituting suprabasal-layer cells that are ultimately shed. We have omitted the dynamics in the suprabasal compartment as these cells do not contribute to tissue maintenance.

$$\begin{array}{lcl}
 P \xrightarrow{\lambda} \begin{cases} P + P & \text{Prob. } r \\ P + D & \text{Prob. } 1 - 2r \\ D + D & \text{Prob. } r \end{cases} & & (1) \\
 D \xrightarrow{\Gamma} \emptyset & &
 \end{array}$$

In order to ensure tissue homeostasis, the probabilities of symmetric divisions that lead to two proliferating cells or two differentiated cells are balanced, i.e. both are defined by a fixed parameter $r \in [0, 0.5]$. This sets a total of three unknown parameters $\theta = \{\lambda, r, \Gamma\}$. Furthermore, under these homeostatic conditions, one can assume that the proportion of progenitor cells in the basal layer, denoted as ρ , remains constant, and overall, the net rate at which post-mitotic cells are generated in the basal layer gets compensated by cell stratification (and shedding), so that $\rho = \Gamma / (\Gamma + \lambda)$. It follows that unless the stratification rate is huge ($\Gamma \gg \lambda$), the basal compartment would still show a substantial level of heterogeneity (with a mixture of both P and D cell pools).

The two independent stem-cell 2XSC model

In this alternative model, derived from Sada et al ³ (see original formulation in **section 5**), two independent stochastic proliferating populations of stem cells are considered (2xSC model). These S_1 and S_2 populations divide at two different rates, $\lambda_{S1} < \lambda_{S2}$, and each follows a pattern of stochastic fate choices similar as in Eq. (1) with a given probability of symmetric division outcome, r_{S1} and r_{S2} , allowing duplication or differentiation. We make the simplifying assumption that $r_{S1} = r_{S2} = r$.

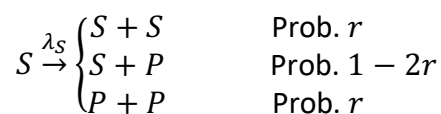


This model yields five adjustable parameters $\theta = \{\lambda_{S1}, \lambda_{S2}, r, \Gamma, \rho_{S1}\}$, where ρ_{S1} is the fraction of slow-dividing stem cells in the basal layer. One can retrieve the proportion of fast-cycling stem cells ρ_{S2} , or the proportion of differentiating cells $\rho_D = 1 - \rho_{S1} - \rho_{S2}$, from the parameter ratios given by the condition of homeostasis. In this way, $\rho_{S2} = (\Gamma - \rho_{S1}(\Gamma + \lambda_{S1})) / (\Gamma + \lambda_{S2})$. Alternatively, we can express the relative fraction of proliferating cells that are slow-cycling stem cells in homeostasis, χ_{S1}^{div} :

$$\chi_{S1}^{div} = \frac{\rho_{S1}(\lambda_{S2} + \Gamma)}{\rho_{S1}(\lambda_{S2} - \lambda_{S1}) + \Gamma} \tag{3}$$

The hierarchical stem cell/committed progenitor model

In this model, introduced by ⁶ and revisited in ⁷, a slow-cycling population of stem cells is considered to underpin the self-renewing dynamics of a second, quickly-dividing population of progenitor cells⁶. Stem (S) cells divide at a slow rate λ_S and undergo stochastic fates, so that they generate, with a certain probability, either two daughter stem cells ($S + S$), two progenitor cells ($P + P$) or one of each ($S + P$). Progenitor cells in turn divide at a faster rate, $\lambda_P \gg \lambda_S$, and commit to stochastic fates too upon division, giving rise to progenitors or differentiating cells as previously indicated. Mascré et al ⁶ made the assumption that $r_S = r_P = r$ (depicted below). In contrast, Sánchez-Danés et al ⁷ assumed these probabilities varied independently.



$$\begin{aligned}
P &\xrightarrow{\lambda_P} \begin{cases} P + P & \text{Prob. } r(1 - \Delta) \\ P + D & \text{Prob. } 1 - 2r \\ D + D & \text{Prob. } r(1 + \Delta) \end{cases} \\
D &\xrightarrow{\Gamma} \emptyset
\end{aligned} \tag{4}$$

The hierarchical proliferative structure makes necessary to introduce a probabilistic bias ($\Delta \in [0, 1]$) in the progenitor daughter fates, so that on average progenitor cells differentiate more often than what they duplicate to compensate for their net production from the stem cell pool and thus guarantee tissue homeostasis. As a result, there are five unknown parameters $\theta = \{\lambda_S, \lambda_P, r, \Gamma, \Delta\}$. The following relationships between parameters can be established at homeostasis:

$$\begin{aligned}
\lambda_S S^{ss} &= 2\lambda_P \Delta r_P P^{ss} \\
\lambda_P P^{ss} (1 + 2\Delta r_P) &= \Gamma D^{ss}
\end{aligned} \tag{5}$$

where S^{ss} , P^{ss} , and D^{ss} represent the bulk populations of stem cells, progenitors and differentiating cells in the basal layer at homeostasis, satisfying the stationary-state conditions $dS/dt = 0$, $dP/dt = 0$, and $dD/dt = 0$, respectively. Rearranging Eq. 5, we get:

$$\begin{aligned}
\rho_S &= \frac{\omega/\lambda_S}{\omega/\lambda_S + 1 + \lambda_P/\Gamma + \omega/\Gamma} \\
\rho_P &= \frac{1}{\omega/\lambda_S + 1 + \lambda_P/\Gamma + \omega/\Gamma} \\
\rho_D &= \frac{\lambda_P/\Gamma + \omega/\Gamma}{\omega/\lambda_S + 1 + \lambda_P/\Gamma + \omega/\Gamma}
\end{aligned} \tag{6}$$

where ρ_x represent the proportion of each x-cell type in the basal layer, and $\omega = 2\lambda_P \Delta r_P$. From here one could deduce the relative fraction of proliferating cells that would represent slow-cycling stem cells in homeostasis, i.e. χ_S^{div} :

$$\chi_S^{div} = \frac{S^{ss}}{S^{ss} + P^{ss}} = \rho_S / (\rho_S + \rho_P) = \frac{\omega}{\omega + \lambda_S} \tag{7}$$

Simulating stochastic clone dynamics under the different hypotheses

In order to explore the range of possible clone dynamics that these different models can offer, we formulated each in terms of its corresponding stochastic Master equation. For instance, for the SP model we have:

$$\tag{8}$$

$$\begin{aligned} \frac{\partial P_{n_P, n_D}}{\partial t} = & \lambda [r(n_P - 1)P_{n_P-1, n_D} + r(n_P + 1)P_{n_P+1, n_D-2} + (1 - 2r)n_P P_{n_P, n_D-1}] \\ & + \Gamma(n_D + 1)P_{n_P, n_D+1} - \lambda n_P P_{n_P, n_D} - \Gamma n_D P_{n_P, n_D} \end{aligned}$$

where $\partial P_{n_P, n_D} / \partial t$ describes the time evolution of the probability of finding clones containing n_P progenitor cells and n_D differentiated cells. Due to the difficulty in computing the analytical solutions for these equations¹¹, in our analyses $P_n(t)$, the probability of each given basal clone size n , was estimated for each model from multiple simulations ($N = 100,000$) of the Master equation, following Gillespie's algorithm by default^{12, 13} (for more elaborated methods, see **sections 3,4**).

As initial condition, we generally set (except when stated otherwise) to start from a random, single labelled proliferative cell, since we can assume that any initially induced differentiating cell will be rapidly swept into the suprabasal compartment and therefore make a negligible contribution to the basal clone dynamics at medium-long term ($t > 1/\Gamma$). In this way, for the SP model: $P_n(0) = \delta_{n_P, 1} \delta_{n_D, 0}$, where $\delta_{n, m}$ represents the Kronecker delta. For the 2xSC model: $P_n(0) = \delta_{n_{S1}, B(1, \chi_{S1}^{div})} \delta_{n_{S2}, B(1, 1 - \chi_{S1}^{div})} \delta_{n_D, 0}$; and for the SC-CP model: $P_n(0) = \delta_{n_S, B(1, \chi_S^{div})} \delta_{n_P, B(1, 1 - \chi_S^{div})} \delta_{n_D, 0}$. Note that $B(m, p)$ represents a random binomial probability term in the two-dividing population models, so that on average, a fraction χ_{S1}^{div} of simulations initiate with a labelled cell targeting the slow-cycling population, and $1 - \chi_{S1}^{div}$ with a quickly-dividing cell, in proportions consistent with the actual ratio of these cell types in homeostasis (Eq. 3 and 7).

All three models show highly similar scaling behaviour. Regardless of the parameter values chosen, clonal dynamics under the SP model adopts the general scaling properties described earlier. In particular, at $t > 1/r\lambda$ the system enters an asymptotic regime¹⁰ where:

$$\begin{aligned} P_{surv}(t) &= \frac{1}{1 + r\lambda t} \\ \langle n \rangle_{surv}(t) &= \frac{1}{\rho} + \frac{r\lambda}{\rho} t \\ P_n^{cum}(t) &= \exp[-n / \langle n \rangle_{surv}(t)] \end{aligned} \tag{9}$$

The exponential scaling of the cumulative clone size frequencies P_n^{cum} yields a linear trend when representing $\log P_n^{cum}(t)$ vs. $n / \langle n \rangle_{surv}(t)$, as observed in oesophageal epithelium (**Supplementary Figure 4D**).

In the 2xSC and SC-CP models, the distribution of basal clone sizes converges to a shape where $\log P_n^{cum}(t)$ does not change fully linearly with the normalized basal clone sizes $n / \langle n \rangle_{surv}(t)$ but displays a biphasic pattern with a U-shaped curve for small clone frequencies due to the mixture of the two different proliferating populations with distinct potential to yield larger clone sizes. However, any deviation from the exponential scaling becomes negligible under

most parameter conditions. Similarly, the average clone size and the fraction of surviving clones of these models adopt curved shapes that show only slight divergence from the single progenitor model for many parameter sets.

Finally, it is worth commenting on the predictions for the evolution of the labelled cell fraction. If the labelled cell fraction faithfully represents the proportions of proliferative cell-types in the homeostatic tissue and an adequate number of clone simulations were initiated from each subpopulation (starting with a single cell, in the way previously stated), the overall population of tracked (labelled) dividing cells across the 100,000 simulations π^{div} remained approximately constant over time, regardless of the model considered. However, these dynamics could become sub-linear or supra-linear under the SC-CP hypothesis insofar as different initial ratios of S and P cells, $\chi_{S,label}^{div}$ and $1 - \chi_{S,label}^{div}$, were tracked than those expressed in Eq. 7. This would reflect a scenario where labelling preferentially targets P cells or S cells, respectively. The time evolution of the labelled cell fraction (omitting the contribution of D cells) would be described by: $d\pi^{div}/Ndt = dS/dt + dP/dt$. Integrating, we get:

$$\pi^{div}(t) = \chi_{S,label}^{div} \left(1 + \frac{\lambda_S}{\omega} (1 - e^{-\omega t}) \right) + (1 - \chi_{S,label}^{div}) e^{-\omega t} \quad (10)$$

This has motivated claims arguing that any deviation from a constant value over time can be attributed to imbalanced fate choices (SC-CP model dynamics, where one could primarily target one or the other dividing subpopulation)⁷. Nevertheless, we note that if we considered a non-negligible fraction of differentiating cells in the basal layer and the possibility of labelling these at a more or less extent, sub-linear or supra-linear trends in the labelled cell fraction could be expected too under the SP model paradigm, if $\rho_{P,label}$ and thus $\rho_{D,label} \equiv 1 - \rho_{P,label}$ were different than the proportions given by ρ in homeostasis. In this case, $d\pi/Ndt = dP/dt + dD/dt$. Integrating:

$$\pi(t) = \rho_{P,label} \left(1 + \frac{\lambda_S}{\Gamma} (1 - e^{-\Gamma t}) \right) + (1 - \rho_{P,label}) e^{-\Gamma t} \quad (11)$$

Notice the similarity of this expression with that in Eq. 10, which relegates the point to a matter of differences in the time scales of the pre-asymptotic behaviour before settling to a constant value.

Altogether, these theoretical modelling results suggest that lineage tracing alone would provide little evidence to support one or another stochastic cell fate model.

3. H2BGFP dilution analysis and inference of homogeneous keratinocyte cell behavior

Since the 2xSC and SC-CP models involve the existence of subpopulations of proliferating cells dividing at different rates, we speculated that we could discriminate between these scenarios and that of the SP model by analyzing the heterogeneity in the pattern of H2BGFP expression of individual keratinocytes during the time course of H2BGFP dilution experiments in transgenic $R26^{M2rtTA}/TetO-H2BGFP$ mice. In this section we describe the experimental details and quantitative modelling involved in this analysis.

Cohorts of at least 2-3 $R26^{M2rtTA}/TetO-H2BGFP$ mice were culled at 0, 7, 12 and 18 days post-doxycycline administration, and the epithelial basal-layer plane imaged from wholemounts of esophagus and hindpaw, ear and tail skin (**Figure 3A-B**). Basal cells were identified as the deepest layer in confocal Z-stacks of epithelial or epidermal tissues (**Supplementary Movies 1-4**). At least 5-8 random fields of view were analyzed per tissue per animal, acquired from distant regions of epithelium. This was to guarantee as much as possible the tissue representativeness and control for possible region-specific differences in the cellular turnover. Samples from back skin epidermis were acquired independently at 0, 5, 11, 14 and 21 days post-doxycycline treatment, corresponding to controls used in another study ⁵. All images were processed with ImageJ to segment nuclear areas (based on DAPI staining) and quantify H2BGFP intensity levels in individual basal keratinocyte nuclei (intensity values were averaged over each nuclear area) (**Supplementary Data 2**). Mitotic cells and CD45⁺ (immune) cells were scored but excluded from the quantitative analysis. Also, immunostaining for Krt14 (a basal keratinocyte marker) helped to exclude suprabasal cells or other cell types from further analysis in tail skin epidermis, which is particularly wavy (**Figure 5A; Supplementary Movie 3**).

Patterns of keratinocyte H2BGFP intensity distributions

If all proliferating keratinocytes behaved as an equivalent population of progenitors dividing at a similar constant rate λ , we would expect a monotonous H2BGFP dilution pattern over time, where all individual-cell fluorescence intensities $I(t)$ would approximately accommodate to a simple exponential decay (recall that the H2BGFP content dilutes two-fold with every cell division):

$$I(t) = I(0) \times 2^{-\lambda t} \quad (12)$$

where $I(0)$ represents the initial cellular H2BGFP intensities. By contrast, if there were subpopulations of keratinocytes dividing at different rates (e.g. $\lambda_s \ll \lambda_p$), these would progressively segregate into different modes in the distribution of H2BGFP intensities at relatively long term, as $t \gg 1/(\lambda_p - \lambda_s)$. A first visual inspection at the experimental data revealed individual-keratinocyte H2BGFP intensities remained overall tightly distributed and scarcely dispersed even at latest 14d-18d time points across the different tissues (**Figure 3C**

and **Figure 4B,D,F**). To formalize and automate the analysis, additional quantitative methods were adopted.

Simulating H2BGFP dilution kinetics under different scenarios of cell proliferation

An initial aim was to explore the quantitative H2BGFP dilution predictions and inference limits set by the different models of cell renewal under reasonable parameter assumptions (**Figure 1D**). For this, we implemented stochastic simulations of the basal cell proliferation dynamics under each of these theoretical scenarios, in a similar manner as in **section 2**, with the peculiarity that simulations were embodied with real distributions of H2BGFP intensities $I(0)$ in the initial cell populations and as individual cell division events occurred, these were linked with two-fold H2BGFP partitioning (**Figure 3E**). An additional noise term was included so that on average H2BGFP content in daughter cells differed by $\sim 10\%$, in agreement with variability observed *in vitro*. Preliminary results using standard Markov-chain Monte-Carlo simulation methods (Gillespie's algorithm) indicated that for common average division rates $\lambda_p \sim 1.5\text{--}3/\text{week}$, a two-to-three weeks chase would be enough to reliably distinguish a 10% subpopulation of basal stem cells dividing at a ≥ 4 -fold slower rate λ_s as a separate, retarded peak in the distribution of H2BGFP intensities.

A major issue of the Markov-chain Monte-Carlo implementations is that they assume kinetic processes are *memoryless*, and therefore, ignore the waiting times between consecutive cell divisions¹⁴. In other words, they consider that the probability that a cell divides in a time interval is independent of its current state and previous time spent in progressing through the cell cycle and only depends on the particular value of λ , so that, for a certain population, the time for completion of the cell cycle t_{cc} satisfies an underlying exponential distribution:

$$P(t_{cc}) \sim \lambda e^{-\lambda t} \quad (13)$$

While this assumption may be acceptable to reproduce long-term dynamics, we found it had major limitations for a realistic description of cellular turnover at short-time scales, as for a given subpopulation with an average cell-cycle period $\langle t_{cc} \rangle = 1/\lambda$, at random, some simulated cells would divide almost immediately after being born while some others would exhibit cell-cycle periods much longer than the average. For this reason, we extended the Monte Carlo algorithm to allow Non-Markovian simulations that permitted to explore alternative, more realistic cell-cycle time distributions (**Figure 3E**; **Supplementary Figure 2A**). In particular, for each subpopulation cycling at a different average rate λ one can implement a delayed exponential distribution¹⁵:

$$P(t_{cc}) \sim \tau_R + \text{Exp}(\varphi) \quad (14)$$

where there would be a refractory period τ_R between consecutive cell divisions (i.e. a minimum cell-cycle time before keratinocytes can commit to divide again). In this case, $\langle t_{cc} \rangle = 1/\lambda = \tau_R + 1/\varphi$. However, more generally, we considered a whole family of hypothetical delayed Gamma distributions for the cell-cycle periods:

$$P(t_{cc}) \sim \tau_R + \text{Gam}(\kappa, \theta) \quad (15)$$

where κ and θ represent the shape and scale parameters of a Gamma distribution. Notice that for $\kappa = 1$, this distribution is a delayed exponential (i.e. Eq. 15 becomes equivalent to Eq. 14) and as κ gets larger, the cell-cycle period distribution would be assumed narrower. In this scenario, $\langle t_{cc} \rangle = 1/\lambda = \tau_R + \kappa\theta$.

The implementation of Gamma-shaped cell-cycle period distributions required modifying the time update process but also the initialization condition in the simulation code to allow for random, asynchronous cell cycle states at the starting time t_0 . This is to guarantee unbiased predictions on dynamics, since division processes would keep *memory* of past events (as opposed to Markovian implementations). In particular, the probability of capturing a cell at a particular time post-division τ would not be uniform but proportional to the probability that longer cell-cycle periods $t_{cc} > \tau$ exist, and follows this equation:

$$\wp(\tau) = C \times \begin{cases} 1 & \tau < \tau_R \\ 1 - \text{GamCDF}(\tau - \tau_R, \kappa, \theta) & \tau \geq \tau_R \end{cases} \quad (16)$$

where C is a normalization factor and GamCDF is the particularized Gamma cumulative distribution function.

By integrating Eq. 16, one can deduce that:

$$\begin{aligned} \wp(0 \leq \tau < \tau_R) &= C \times \tau_R \\ \wp(\tau_R \leq \tau < \infty) &= C \times \int_{\tau_R}^{\infty} (1 - \text{GamCDF}(\tau - \tau_R)) d\tau \end{aligned} \quad (17)$$

Accordingly, in the simulations, initial cells were assigned random cell-cycle states τ drawn from the corresponding underlying distributions (Eq. 16 and Eq. 17), so that a certain fraction were realistically ascribed to early stages of the cell-cycle ($\tau < \tau_R$) and thus required longer to undergo the first round of division (and therefore start the H2BGFP content dilution).

Following this refined methodology, we explored the H2BGFP dilution pattern predictions $I(t)$ in different theoretical scenarios, including the SC-CP and 2xSC models under the corresponding parameter conditions set by ⁶, and ³. Taking assumptions on the underlying cell-cycle time distributions in agreement with common estimates provided below (for quickly-dividing cells: $\tau_R = 0.5d$, $\kappa = 8$; for slow-cycling cells: $\tau_R = 0.1 \times \langle t_{cc} \rangle$, $\kappa = 8$), we found

all these previous cases involving heterogeneous populations of slow- and quickly- dividing cells would lead to separated peaks in H2BGFP histograms by three weeks, in contrast to SP model predictions where individual-cell H2BGFP distributions would remain as a single peak (**Figure 4A**).

Unimodality tests and cell-proliferation model inference

In order to formalize the classification of H2BGFP dilution patterns and test the efficiency to discriminate between homogeneous and heterogeneous proliferating cell population hypotheses, we next applied multiple statistical tests for unimodality. Six different methods were considered: Hartigan & Hartigan (1985) dip test (HH) ¹⁶, Silverman (1981) critical bandwidth test (SI) ¹⁷, Cheng & Hall (1998) excess mass test (CH) ¹⁸, Hall & York (2001) critical bandwidth test (HY) ¹⁹, Fisher & Marron (2001) Cramer-von Mises test (FM) ²⁰ and Ameijeiras-Alonso et al (2018) excess mass test (ACR) ²¹. All these tests yielded significant p-values for the H2BGFP distributions of the SC-CP and 2xSC scenarios set above, classifying them as multimodal (**Figure 4A**).

Having demonstrated the reliability on synthetic data sets, we applied the unimodality tests to the experimental data to estimate the likelihood that the evolving fluorescence intensity distributions arose from a single proliferating cell population or cells dividing at multiple rates. Empirical distributions remained largely unimodal over time across body sites, both by analysing individual mice-derived data (**Figure 3D**) or individual fields of view separately (**Supplementary Data 3**). ~5 % of all samples were identified as multimodal based on $p=0.05$ (without multiple comparison correction). We found that there was no clear relationship between collection time and multimodality, and that, when observed, multimodality was inconsistent between animals. Furthermore, regardless of collection time, cell subpopulations classified as multimodal differed in a single division round, suggesting that the time of collection for those animals could occur during progression of synchronised divisions.

The analyses performed per field of view more strongly favoured unimodality than the individual animal measures, suggesting minor spatial asynchronies in the cell division timing (**Figure 5C**). Altogether, our data are consistent with a single average rate of cell division λ at any given site, supporting the simplest SP model paradigm throughout the oesophagus and different skin niches.

Estimating the distribution of keratinocyte cell-cycle times

To further validate the SP model, we fit models of cell-cycle time distributions to the observed H2BGFP intensity profiles over time. If a unique mode of cell proliferation prevailed across the entire population of keratinocytes, the full shape of the cellular H2BGFP distributions at

different times would be reproducible by means of a model distribution of cell-cycle periods (Eq. 15).

A grid-based Approximate Bayesian Computation (ABC) rejection method ²², was implemented to fit the time series of experimental H2BGFP intensity distributions with results from SP model simulations varying the values of the unknown cell-cycle parameters τ_R and κ . In this methodology for each tissue we fixed the value of the parameter λ ($\lambda = 2.9, 2.0, 1.5, 1.2/\text{week}$ for oesophagus, hind-paw, ear and dorsum, respectively; estimated from the linear slope in the semi-logarithmic plot showing $\log(I)$ vs. time; see Eq. 12). Basal cell H2BGFP content dilution was simulated starting from initial values drawn from the corresponding empirical $I(0)$ distribution, used as prior, and similar assumptions on label partitioning were considered as the ones described above.

A distance metric was computed for every $\{\tau_R, \kappa\}$ value pair based on the sum of absolute quantile differences between the simulated and the empirical $I(t)$ histograms at the different time points, using quantiles taken at 0.025, 0.25, 0.5, 0.75, and 0.975. This identified a family of acceptable shapes for the cell-cycle period distribution, obtained as posterior estimates (**Figure 3G; Figure 4 C,E,G**). In agreement with the SP paradigm, we obtained adequate fits on the whole series of keratinocyte H2BGFP dilution patterns with the following cell-cycle attributes: $\{\tau_R = 0.5, 1.0, 0.5, 0.5 \text{ days}; \kappa = 8, 4, 8, 16\}$ for oesophagus, hind-paw, ear and dorsum, respectively (**Figure 3C; Figure 4 B,D,F; Supplementary Data 4**). Note using the outcome of a Kolmogorov-Smirnov test as an alternative distance metric did not substantially alter the cell-cycle solutions.

4. Single-progenitor parameter inference from clonal data sets

Nine independent lineage-tracing data sets were exploited to challenge the suitability of the SP model to explain clonal dynamics in the esophagus and the different skin territories, and ultimately infer the most-likely parameter values of keratinocyte cell behavior. Given the diverse methodologies and disparity of inference results described so far in the literature (see **section 5**), we decided to undertake a single, robust, maximum likelihood estimation (MLE) approach for model fitting across data sets. In particular, a comprehensive grid search was performed on the unknown SP model parameters, and for every set of parameter values θ we run multiple simulations (see below) to get a theoretical estimate of the time course in the basal clone size distributions, to be contrasted with the experimental one. A log-likelihood value $l(\theta; x)$ was calculated as follows:

$$l(\theta; x) = \sum_t \sum_n (x_n(t) * \log p_n(t, \theta)) \quad (18)$$

where $x_n(t)$ is the observed frequency of clones of a certain basal size n at time t , and $p_n(t, \theta)$ is the probability of observing clones of that size at time t given the parameter values θ , a quantity obtained from the model simulations.

Note that, given the particular scaling behavior of the clone size distributions and their large asymmetry (approximately log-normal-like shapes), clone sizes were conveniently binned in ranges increasing in powers of two, as done in previous work ⁵, i.e. n above stands for clones with a number of basal cells in the range $(2^{n-1} + 1)$ to 2^n . Also, only surviving clones with at least 2 basal cells were considered for the MLE analysis, to exclude any possible contribution due to post-mitotic cells labelled at induction (recall the initialization condition for simulations was $P_n(t_0) = \delta_{n_P,1} \delta_{n_D,0}$). Additionally, in some experimental data sets a small proportion (<1%) of late-time clones were reported with sizes that greatly exceeded the vast majority of their coexisting clones (i.e. sizes $\gg 2.3 \times \text{SD}$ above the mean clone size, a reference for the 99% CI threshold of log-normal distributions). This occurred for 3, 4 and 5 clones in the data sets from esophagus ¹, dorsum ⁵ and paw ⁸, respectively. These outlier clones, which could be interpreted as a result of non-neutrality or coincidental fusion between two adjacent clones, were pooled together and assigned into the immediate prior category of clone sizes to circumvent the computational issues of estimating the probability of extremely rare events with sufficient precision. However, excluding these outstandingly large clones from the analysis did not substantially alter the parameter estimates provided below.

Maximum likelihood estimates $\hat{\theta}_{MLE}$ (maximizing the expression in Eq. 18) were obtained for each data set, and presented with 95% confidence intervals computed based on the likelihood-ratio test ²¹. Parameter solutions were plotted as heatmaps in 2D or 3D parameter spaces (as applicable), color coded according to the value of the log-likelihood ratio statistic (the maximum value of 0 corresponding with the $\hat{\theta}_{MLE}$). Parameter sets with values falling below -7.81 (the χ^2 statistic cutoff for an $\alpha=0.05$, 3 degrees of freedom) were considered non-optimal and generally not displayed.

Cell cycle time constrained parameter inference

As a first approximation to parameter inference, simulations were performed using Gillespie's Markov-chain Monte-Carlo algorithm (as described in **section 2**) and all the 3 parameters of the SP model were considered unknown (**Supplementary Figure 1A**). We thus iterated on values of $r \in [0, 0.5]$, $\rho \in [0, 1]$ and λ (within a reasonable range of values: $\in [0.4, 3.6]/\text{week}$) (recall $\rho = \Gamma / (\Gamma + \lambda)$ in homeostasis), testing a total of $\sim 230,000$ parameter conditions in a 3D space (super-computing resources at the Wellcome Sanger Institute were used for parallelization). Multiple parameter combinations yielded relatively good fits on clone size distributions over time (**Supplementary Figure 1A-B**). λ may be accurately measured independently by H2BGFP dilution experiments (**section 3**), so that, in practice, we used this estimate to constrain our parameter search to 2D (a total of 101×100 parameter

combinations were explored). By this means, we increased the discrimination on the values of the parameters r and ρ (or Γ), yet a certain level of imprecision remained among solutions aligning around constant r/ρ ratios, leaving a characteristic, relatively long trail of coloured patterns in the corresponding heatmaps (**Supplementary Figure 1C**) (see below).

One could potentially speculate if this level of parameter imprecision was due to biological variability (e.g. inter-mice differences or age-related differences in cell behaviour across the distinct time points). However, we separated the MLE calculation into individual time point analyses, observing each was consistent with a similar pattern of degenerated solutions (**Supplementary Figure 1C**, upper panels). We also generated synthetic data sets by strict simulation of the SP model under specific parameter values and submitted their clone size distributions to a similar MLE inference analysis, obtaining comparable levels of inaccuracy for same sample sizes (**Supplementary Figure 1C**, bottom panels). This suggested that parameter uncertainty was not biological, nor due to a flawed, inappropriate SP-model definition. We highlight in the different experimental heatmap panels how the direction in our MLE parameter uncertainties fell indeed consistent with the r/ρ ratios obtained from the asymptotic linear slope in the average clone size over time (**Figure 7D**, grey lines) (dashed lines correspond with the 95% CI limits in the linear slope). It follows that it is an inherent feature of the stochastic nature of clone fates and their quick convergence into a scaling form, as extended synthetic data sets revealed: the level of imprecision could in theory be further attenuated by larger experimental sample sizes at relatively early time points (**Supplementary Figure 1D**).

A second issue arises from the possible impact the assumptions on the cell-cycle time distribution may have on clone-size estimates and hence on parameter inference. For that reason, Non-Markovian simulations of the SP model were tested, with different hypothetical underlying cell-cycle time distributions, as we did in **section 3** for cell-proliferation studies (**Supplementary Figure 2A**). Theoretical simulation results confirmed clone size frequencies predicted at relatively early time points differed substantially between implementations carried out with Gamma-distributed cell-cycle periods and those with default exponential assumptions, differences getting smaller over time, as shown by Kullback–Leibler divergence (**Supplementary Figure 2B-C**). On average, it was not until a critical time T_c of $3(2; 10) \times \langle t_{cc} \rangle$ that details of the shape of cell-cycle time distribution became unimportant on clonal predictions. This meant the shortest experimental time points, when clonal data have not yet fully converged to the long-term scaling behavior and can potentially improve the precision of estimated cell parameters, were also more prone to contribute to a biased inference given unrealistic assumptions on the cell-cycle time distribution (**Supplementary Figure 2D-E**). Therefore, our SP model simulations used for MLE parameter inference were constrained for each body site by the actual cell-cycle time distribution estimated from the corresponding H2BGFP dilution analysis (**section 3**) (**Figure 6**).

Following this more realistic methodology, the SP parameter estimates $\hat{\theta}_{MLE}$ generally shifted towards lower values of ρ (and a slower stratification rate Γ) than those predicted with default Markovian simulations (i.e. exponential t_{cc} distributions), discarding hypothetical scenarios where differentiating cells would be largely absent in the basal compartment and would stratify almost immediately after being born (**Figure 7D**). Excellent fits were obtained on the time courses of the experimental clone size distributions -including early and long-term clonal behavior- across data sets, resulting in a statistically significant improvement over the model predictions made by the original publications (**Figure 7E**; **Figure 8A-C**; **Supplementary Data 4**). Compared to our $\hat{\theta}_{MLE}$, the value of the log-likelihood ratio statistic of previous estimates was: -9.4 (for Doupé et al's ¹ fits in esophagus), -364.2 (for Lim et al's ¹ fits in hind-paw epidermis), -29.3 (for Doupé et al's fits in ear epidermis ²³) and -13.0 (for Murai et al's fits in dorsal epidermis ⁵). Altogether, our fits confirm the suitability of the SP model and provide more accurate descriptions of the parameters defining keratinocyte cell behavior in the different territories (**Table 1**).

5. Revisiting alternative datasets and interpretations

Here we revisit published work from the literature in order to test the ability of a cell-cycle time-sensitive SP model to explain these different datasets, and we reexamine the specific arguments and claims previously given in support of alternative models.

Doupé et al (2012), esophageal epithelium¹

In Doupé et al. we first studied the validity of the SP model in the mouse esophageal epithelium, by lineage tracing using *Ah-Cre^{ER} R26^{EYFP}* mice. An analytical approximation was then followed to solve the theoretical clone size likelihoods and Bayesian inference used for SP model parameter estimation. The estimate for $\lambda = 2/\text{week}$ at that time was congruent with an independent H2BGFP dilution experiment, even though we now consider that the poor late-time H2BGFP signal-to-noise ratio on that occasion could lead us to underestimate the true division rate. In the present study we got a higher average division rate $\lambda = 3/\text{week}$ with new technology and more animals and time points (**Figure 3**). This fact as well as the consideration of Gamma-distributed cell-cycle periods made our new parameter estimates to slightly deviate from those reported in Doupé et al (**Figure 7D,E**; **section 4**).

Giroux et al (2017), esophageal epithelium²

Giroux et al performed lineage tracing in mouse esophageal epithelium using a *Krt15* promoter, and postulated the existence of a long-lived subpopulation of stem cells, characterized by high expression of KRT15. The authors concluded on the heterogeneous proliferation potential of the esophageal basal cells –a scenario compatible with a hierarchical stem-cell transit-amplifying cell model – based on the molecular properties of the Krt15⁺ basal

cells and the long-term persistence of a subset of *Krt15*-labelled clones well beyond the homeostatic renewal time of the epithelium, giving rise to all differentiated lineages. This observation is however consistent with the SP model, since, as noted above, a small number of clones dominate the tissue after extended periods. Giroux et al did not report clone sizes, but data on clonal densities could be recovered from presented figures. Using these experimental lineage-tracing results in *Krt15-Cre^{PR1} R26^{mT/mG}* mice as an independent dataset, we found that the single progenitor model proposed for the esophagus was indeed capable of reproducing observed data. The best parameter estimates obtained from the analysis of *Lrig1-eGFPcre^{ERT} R26^{flConfetti}* clones produced excellent fits on the time course in the *Krt15*-labelled clone density from²(**Supplementary Figure 4F, left panel; Supplementary Data 4**). Finally, we extended our analysis to consider the label distribution across differentiated cell layers (Fig. 2E in ²). Again, we observed the SP predictions were consistent with experimental observations (**Supplementary Figure 4F, right panel; Supplementary Data 4**), indicating that a hierarchy is not required to explain esophageal epithelium dynamics.

Mascre et al (2012) and the SC-CP model

Mascre et al propose a proliferative hierarchy of slow-cycling stem cells underpinning committed progenitor cells (SC-CP model) from the quantitative analysis of clonal fates in the tail interfollicular epidermis. The authors argue that cells labelled with two different inducible genetic constructs targeting the promoters *Irf1* and *Krt14* have distinct dynamics. They conclude that *Irf1* and *Krt14* are markers of P cells and both P and S cell populations, respectively. However, in this paper the authors did not test the ability of alternative models to describe the observed data. The SC-CP model was explicitly claimed to explain the diverging trends in the surviving clone fraction and the labelled cell fates at the earliest time points.

Unfortunately, the clonal data was not available. Alternatively, cell proliferation-related data could be extracted from plots of an independent H2BGFP dilution experiment performed to validate their predictions. We reanalyzed the displayed distributions of the number of cell divisions (see Fig. 3k in ⁵) and found that a SP model ($\lambda = 1.3/\text{week}$; cell-cycle distribution with $\tau_R = 0.6$ days, $\kappa = 1.5$) (**Supplementary Data S4**) could provide a similar, suitable fit on the experimental data along the different chase times (**Supplementary Figure 6A**). Furthermore, no bimodality was observed in the distribution of histone intensities, as one might expect by the 3 week timepoint if there was a significant subpopulation of slow-cycling stem cells dividing at $\lambda_S \approx 0.1/\text{week}$ (**Figure 4A; section 3**).

A limitation for this study is that the structural heterogeneity of murine tail was not considered, when distinct spatial territories (scale and interscale regions; **Figure 5A**) are believed to show different developmental processes, cell proliferation rates, and differentiation programs²⁴. As in ³, this spatial information was not considered in ⁵, where H2BGFP fluorescence was analyzed from FACS on pools of basal (α_6 -integrin+ CD34-) cells.

Another potential issue was that no labelling and exclusion of immune, CD45+ cells was performed in the study of label retaining cells, which could introduce a source of error.

Sánchez-Danés et al (2016), tail skin

As a continuation to the work in Mascré et al ^{5 6} revisited clonal dynamics in tail skin by inducible genetic labeling using same targeted promoters, *lvi* and *Krt14*, but analyzing labelled clones independently in scale and interscale regions. While they conclude that a SP model explains clonal dynamics in scale, they argue the SC-CP model prevails in interscale on the basis of the different clonal dynamics observed using the *lvi-Cre^{ER}* and *Krt14-Cre^{ER}* constructs. The evidence used to make this argument is an apparent decrease in the labelled cell fraction over time for the *lvi-Cre^{ER}*-targeted population (argued to only label committed progenitors), and an increase in the labelled cell fraction of the *Krt14-Cre^{ER}*-targeted clones (considered to comprise driving stem cells) (see Fig. 2e in ⁶) (Eq. 10). Here, the labelled cell fraction was *estimated* as a product of the average basal clone size and the overall clone density, which is discussed later.

For the purpose of model fitting and validation they assumed division rates for the P cells similar to those reported in ⁵ in both scale or interscale regions ($\lambda_P \approx 1.2/\text{week}$). A least-squares minimization procedure was then used to fit the evolution of the mean clone sizes for each construct in each compartment, using the corresponding ascribed model, either the SP or the SC-CP model. They found the best fit for the labelled *Krt14-Cre^{ER}* clones in interscale was attained with a SC-CP model where $\lambda_S = 0.45/\text{week}$, $r_S = 0.03$, $\lambda_P = 1.7/\text{week}$, $r_P = 0.19$, $\Delta = 0.02$ and $\chi_{S,label}^{div} = 0.65$ (see Fig. 2d in ⁶). The confidence intervals in the value of Δ span the $\Delta = 0$ condition, suggesting that a fit on clonal dynamics would be possible without P cells showing a necessary imbalance towards terminal differentiation, raising the question of whether a SP model could recapitulate the data.

We therefore fitted the experimental basal clone size distributions ⁶ with a SP model, taking $\lambda_P = 1.2/\text{week}$, as in ⁵. The best-fit parameter sets showed improved fits on both the scale- and interscale- *Krt14-Cre^{ER}* clone data (**Supplementary Figure 6B; Supplementary Data 4**). Our results for interscale demonstrate that a SP model ($\lambda_P = 1.2/\text{week}$, $r = 0.09$, $\Gamma = 2.2/\text{week}$) showed satisfactory fittings on the clone size frequencies, average clone size and clonal survival over time (**Supplementary Figure 6B-D**).

Given that time courses in clone size and clonal survival are both consistent with the SP model, it is sensible to consider whether the apparent trends in the labelled cell fraction can also be explained within this paradigm. While the labelling of a large, representative set of dividing cells in homeostasis would in principle remain overall constant over time, there are two possible sources of variation that could contribute to the observed deviations with the SP model: stochastic growth or decline in a finite labelled population, and inter-animal

variation in initial label induction. To address the question of whether these sources of random variation could be sufficient to explain the extent of increase in the *Krt14-Cre^{ER}*-labelled cell fraction, we reexamined noise by *error propagation* in both the original data and simulated SP model.

To account for inter-animal variation in label efficiency, we measured SD from clonal density data by exclusively studying a single, arbitrarily selected sub-region per animal ($N = 2-5$ mice per time point). In the original study, multiple distinct sub-regions were treated as independent observations, reducing the apparent error arising from variable labelling. The SD in clone density was then integrated together with the SEM in basal clone size to obtain the experimental error in the *estimated* label cell fraction at each time. To estimate variations in average clone size due to SP stochasticity, we subsequently run time-course simulations tracking the same number of clones counted in the experiments ($N = 72, 75, 40, 31, 47, 70$ clones sampled at time 1, 2, 4, 8, 12 and 24w, respectively), and measured the SEM and average clone size obtained through multiple runs. This info was combined with independent time-course simulations of clone density reproducing the variable clonal induction. From this analysis we find that any trend in the experimental *Krt14-Cre^{ER}*-labelled cell population from ⁶ largely fell within the domain of uncertainty given by the combined sources of variation, considering the actual level of sampling error, with just the very last time point being at the borderline of the 95% confidence interval (**Supplementary Figure 6E**).

Finally, given that *Krt14-Cre^{ER}* clonal dynamics can be explained by the SP model, it raises the question of how distinct the *Ivl-Cre^{ER}* interscale clone population behavior is. Indeed, excluding the earliest two experimental time points (up to 2 weeks post-induction, where dynamics could be potentially influenced by initial priming of labelled cells towards differentiation; recall Eq. 11), we find an adequate fit over the time courses in the average clone size, clonal survival and labelled cell fraction with just the same parameter values obtained from fitting *Krt14-Cre^{ER}* populations (**Supplementary Figure 6F-H; Supplementary Data 4**). This suggests that two distinct promoters could target the same, unique proliferative cell type.

Sada et al (2016) and the 2xSC model

Sada et al ³ propose a model of epithelial cell renewal where tissue is maintained by two independent populations of dividing stem cells cycling at different rates (2xSC model). This model was based upon observations made in H2B-GFP dilution experiments in back-skin keratinocytes. In these experiments the authors tracked H2B-GFP histograms of FACS-sorted epidermal cells from *Krt14-cre^{ERT} R26^{tdTomato} Krt5^{tTA}/pTRE-H2BGFP* mice collected after different chase times with doxycycline (**Supplementary Figure 5A**).

Based on this experiment, the authors reported resolved distributions of the number of cell divisions for the basal, spinous and granular layers separately. They further attempted to fit different published models to the data, finding that neither the SP-model nor the SC-CP model adequately described the data, whilst the 2xSC model was compatible (see Fig. 3 in ⁴). Here we examine their model *implementation* (in contrast to the more general mathematical description given in **section 2**).

In their model, the authors considered two subpopulations of basal cells, S_1 and S_2 . Cells in the S_2 population may either divide or stratify. Division occurs slowly, giving two S_2 daughter cells, and stratification is conceived as an independent, “division-uncoupled” process. That is to say, cell fate is not determined on birth. We note that this subpopulation would in fact behave equivalently to a constrained SP-model where $r=0.25$ (e.g. see ¹²). The authors’ decision to consider S_2 basal cells as a single pool undergoing symmetric divisions is perhaps arbitrary, since in homeostasis half of these cells should go on to divide and half should stratify (i.e. can be called D-cells), hence the reason for $r=0.25$ using the SP-model formulation (Eq. 1). Regardless of whether biological differentiation initiates prior to, concomitantly to, or after stratification, a class of basal “D” cells (ignored by the authors) arising from the S_2 population can be defined *post hoc*, as those cells that proceed to stratify (as described above in **section 2**). Thus, the time of fate determination does not alter the model formulation and S_2 cells can be considered as a stochastic SP population (Eq. 1).

S_1 cells in contrast divide quickly and asymmetrically, giving one S_1 daughter and one stratifying, suprabasal daughter, implying any differentiating D cell stratifies immediately upon birth (“division-coupled stratification”). This is a deterministic process of invariant asymmetric self-renewal, and as such, would not be supported by clone size distributions observed in lineage tracing experiments (see **section 2**).

To resolve this issue, the authors introduce a variant of the 2xSC model (termed the “hybrid” 2xSC model, as opposed to the former “semi-coupled” one) where the S_1 population undergoes a combination of symmetric and asymmetric divisions. It follows that S_1 differentiating cells should stochastically choose between waiting and following an uncoupled stratification process (with probability u_{S1}) or stratifying immediately after division (with probability $1 - u_{S1}$). We note that whilst this new complex mechanism could reproduce clone size distributions, there exists no direct evidence to support it.

The hybrid 2xSC model was directly implemented using the following differential equations to account for H2B-GFP dilution kinetics (pg.14-16 in Supplementary Note in ⁴):

$$\begin{aligned} D_t \eta_d^{S1}(t) &= (1 + u_{S1}) \lambda_{S1} \eta_{d-1}^{S1}(t) - (\lambda_{S1} + u_{S1} k_{S1 \rightarrow SL}) \eta_d^{S1}(t) \\ D_t \eta_d^{S2}(t) &= 2 \lambda_{S2} \eta_{d-1}^{S2}(t) - (\lambda_{S2} + k_{S2 \rightarrow SL}) \eta_d^{S2}(t) \\ D_t \eta_d^{SL}(t) &= u_{S1} k_{S1 \rightarrow SL} \eta_d^{S1}(t) + (1 - u_{S1}) \lambda_{S1} \eta_{d-1}^{S1}(t) + k_{S2 \rightarrow SL} \eta_d^{S2}(t) - k_{SL \rightarrow GL} \eta_d^{SL}(t) \end{aligned} \quad (19)$$

subjected to boundary conditions $\eta_d^x(0) = \delta_{d0}\rho_x$, where $\eta_d^x(t)$ represents the density of cells of type x that have divided d times by time t . In the extreme, semi-coupled scenario ($u_{S1} = 0$), the equations were reported as:

$$\begin{aligned} D_t \eta_d^{S1}(t) &= \lambda_{S1} (\eta_{d-1}^{S1}(t) - \eta_d^{S1}(t)) \\ D_t \eta_d^{S2}(t) &= 2\lambda_{S2} \eta_{d-1}^{S2}(t) - (\lambda_{S2} + k_{S2 \rightarrow SL}) \eta_d^{S2}(t) \\ D_t \eta_d^{SL}(t) &= \lambda_{S1} \eta_{d-1}^{S1}(t) + k_{S2 \rightarrow SL} \eta_d^{S2}(t) - k_{SL \rightarrow GL} \eta_d^{SL}(t) \end{aligned} \quad (20)$$

In a later refinement, the authors replaced the S_1 and SL processes by two-step Poisson processes involving two subpopulations, each having twice the rate of the original process, in order to recreate Gamma waiting-time distributions ($\kappa=2$). This final model was the one used to fit to the experimental data, and thus the one we reassessed. Nevertheless, our main points below arise from the core implementation, and apply irrespective of waiting-time considerations, reason why we present equations as in their simple version for clarity.

Here, we reimplemented Sada et al's model to test its properties. To do so, we first displayed the hybrid 2xSC model mathematically, in terms of its constituent processes and associated transition probabilities:

$$\begin{aligned} S_1 &\rightarrow \begin{cases} \xrightarrow{\lambda_{S1}} S_1 + S_1 & \text{Prob. } u_{S1}/(1 + u_{S1}) \\ \xrightarrow{\lambda_{S1}} S_1 + SL & \text{Prob. } (1 - u_{S1})/(1 + u_{S1}) \\ \xrightarrow{k_{S1 \rightarrow SL}} SL & \text{Prob. } u_{S1}/(1 + u_{S1}) \end{cases} \\ S_2 &\rightarrow \begin{cases} \xrightarrow{\lambda_{S2}} S_2 + S_2 & \text{Prob. 0.5} \\ \xrightarrow{k_{S2 \rightarrow SL}} SL & \text{Prob. 0.5} \end{cases} \\ SL &\xrightarrow{k_{SL \rightarrow GL}} \emptyset \end{aligned} \quad (21)$$

where λ_{S1} , $k_{S1 \rightarrow SL}$, and λ_{S2} , $k_{S2 \rightarrow SL}$ denote the division and stratification rates of the S_1 and S_2 populations, respectively. SL refers to the population of cells in the first suprabasal (spinous) compartment, which would transit with rate $k_{SL \rightarrow GL}$ to the granular layer and to more external layers successively (here not depicted). In homeostasis, $k_{S1 \rightarrow SL} = \lambda_{S1}$, $k_{S2 \rightarrow SL} = \lambda_{S2}$, and $k_{SL \rightarrow GL} = (\lambda_{S1} \chi_{S1}^{div} / (1 + u_{S1}) + 0.5 \lambda_{S2} (1 - \chi_{S1}^{div})) / m$, where χ_{S1}^{div} is the fraction of S_1 basal cells and m is the spinous suprabasal-to-basal cell ratio. The event probability terms in Eq. 21 are those required for homeostasis. From Eq. 21 it becomes apparent how Sada et al's hybrid 2xSC model represents a particular case of a two SP model combination where $r_{S2} = 0.25$, $r_{S1} = u_{S1}/(1+u_{S1})$ and $\Gamma \rightarrow \infty$ (i.e. differentiating D-cells stratifying immediately upon birth to yield SL cells). That is why in **section 2** we adopted the more general form to represent the 2xSC

model (Eq. 2) (in that case we referred to the slow-cycling population as S_1 for convenient comparison with SP and SC-CP schemes).

When we derive the kinetic equations for H2B-GFP dilution analysis from Eq. 21 we obtain:

$$\begin{aligned} D_t \eta_d^{S_1}(t) &= \lambda_{S_1} \eta_{d-1}^{S_1}(t) - \left(\frac{1}{1+u_{S_1}} \lambda_{S_1} + \frac{u_{S_1}}{1+u_{S_1}} k_{S_1 \rightarrow SL} \right) \eta_d^{S_1}(t) \\ D_t \eta_d^{S_2}(t) &= \lambda_{S_2} \eta_{d-1}^{S_2}(t) - 0.5(\lambda_{S_2} + k_{S_2 \rightarrow SL}) \eta_d^{S_2}(t) \\ D_t \eta_d^{SL}(t) &= \frac{u_{S_1}}{1+u_{S_1}} k_{S_1 \rightarrow SL} \eta_d^{S_1}(t) + \frac{1-u_{S_1}}{1+u_{S_1}} \lambda_{S_1} \eta_{d-1}^{S_1}(t) + 0.5 k_{S_2 \rightarrow SL} \eta_d^{S_2}(t) - k_{SL \rightarrow GL} \eta_d^{SL}(t) \end{aligned} \quad (22)$$

For $u_{S_1} = 0$ (semi-coupled case), these simplify to:

$$\begin{aligned} D_t \eta_d^{S_1}(t) &= \lambda_{S_1} (\eta_{d-1}^{S_1}(t) - \eta_d^{S_1}(t)) \\ D_t \eta_d^{S_2}(t) &= \lambda_{S_2} \eta_{d-1}^{S_2}(t) - 0.5(\lambda_{S_2} + k_{S_2 \rightarrow SL}) \eta_d^{S_2}(t) \\ D_t \eta_d^{SL}(t) &= \lambda_{S_1} \eta_{d-1}^{S_1}(t) + 0.5 k_{S_2 \rightarrow SL} \eta_d^{S_2}(t) - k_{SL \rightarrow GL} \eta_d^{SL}(t) \end{aligned} \quad (23)$$

Comparing Eq. 22-23 with Eq. 19-20, we observe that Sada et al³ omitted some probability terms in their equations; most noticeably the 0.5 factor accompanying the λ_{S_2} parameter, which could have potentially impacted on the estimates given for S_2 the division rate. To shed light on this, we simulated H2BGFP dilution kinetics of the 2xSC model, taking the estimated parameter values from in the paper⁴: $\lambda_{S_1} = 0.47/\text{day}$, $\lambda_{S_2} = 0.19/\text{day}$, $u_{S_1} = 0.20$, $\chi_{S_1}^{div} = 0.74$. We found that we were unable to reproduce the reported fittings on the distributions of cell division number. In fact, these conditions resulted in bimodal H2BGFP dilution profiles and very poor fits against their experimental data (**Supplementary Figure 5B**: dashed blue lines) (This bimodality becomes even more prominent when considering narrower cell-cycle time distributions comparable to those we find in our experiments (**Figure 4A**)). In contrast, when keeping all other constants equal but using $\lambda_{S_2} = 0.38/\text{day}$ (a value twice the one reported), we found that the model fitted the data well, consistent with the fits originally presented by the authors, suggesting that the reported value for λ_{S_2} was incorrectly half of the actual rate (**Supplementary Figure 5B**: solid blue lines). To corroborate these findings, our analysis was performed both by stochastic simulation of processes in Eq. 21 (following the methods described in **section 3**) and by numerical integration of Eq. 22-23, obtaining the same results.

In light of the apparently similar rates of division for the S_1 and S_2 populations ($\lambda_{S_1} \approx 3.3/\text{week}$ and $\lambda_{S_2} \approx 2.7/\text{week}$), we reinvestigated whether the SP model could provide an adequate fit of the data. Whilst the authors reported poor fits with a SP model (**Supplementary Figure 5B**: dashed orange lines), this model was just tested assuming rates could be adequately modelled as Poisson processes, whereas the 2xSC model was implemented using Gamma distribution waiting-time processes. As explored in **section 3**, the choice of distribution for

cell-cycle times can substantially alter fits for histone dilution experiments, and we therefore took account of this explicitly.

Using the methods described in **section 3**, we explored different rates and waiting time values for the SP model and obtained fits similarly good as with the 2xSC model with a single population with division rate $\lambda = 3.1/\text{week}$ with a minimum refractory period $\tau_R = 0.4$ days, and a stratification rate $\Gamma = k_{SL \rightarrow GL} = 16 \times \lambda$ following a Gamma distribution with shape parameter $\kappa_{\text{strat}} = 2.8$ (**Supplementary Figure 5B**: solid orange lines; **Supplementary Data 4**). We therefore conclude that the SP model proves suitable to explain the dataset in ³.

Füllgrabe et al (2015), back skin ⁴

Füllgrabe et al performed genetic lineage tracing followed by quantitative analysis of clone dynamics from *Lgr6*-expressing back-skin cells, observing scaling properties indicative of stochastic, population asymmetry self-renewal in the interfollicular epidermis of murine dorsum. Although the authors did not attempt a detailed model verification/parameterization, we considered the lineage tracing outcome from *Lgr6-cre^{ERT}/R26^{Confetti}* mice could constitute an ideal independent dataset to challenge our SP-model predictions against. Given the fact that labelling of *Lgr6*+ cells was induced early in postnatal development (P3w), at a time when the tissue was likely not yet homeostatic (see Fig. 1D in ⁴), we restricted the analysis to the late time points where mice were at least 8w old and the tissue was representative of adulthood. To do so, we randomly sampled the observed clone sizes at 40 days post-induction as initial modelling condition and simulated clonal dynamics over the period up to the 100-days and 150-days timepoints using a SP model with the parameters inferred from the H2B-GFP pulse-chase (**Figure 4F-G**) and *Ah-cre^{ERT}/R26^{EYFP}* system (**Figure 8C**; **Table 1**; **Supplementary Data 4**). To take account of the unknown composition of initial preformed clones, we randomized (according to a binomial distribution) the proportion of P-cells in each simulated initial clone according with the parameter $p = 0.61$.

Our fits fell in agreement with the observed growth in the average clone size as well as with the experimental time courses in the frequencies of clone sizes (**Supplementary Figure 5C**). These results reaffirm the validity of the SP paradigm in murine back skin with the parameter values we calculated previously, using an independent genetic construct.

Supplementary references

1. Doupe, D.P. *et al.* A single progenitor population switches behavior to maintain and repair esophageal epithelium. *Science* **337**, 1091-1093 (2012).
2. Giroux, V. *et al.* Long-lived keratin 15+ esophageal progenitor cells contribute to homeostasis and regeneration. *J Clin Invest* **127**, 2378-2391 (2017).
3. Sada, A. *et al.* Defining the cellular lineage hierarchy in the interfollicular epidermis of adult skin. *Nat Cell Biol* **18**, 619-631 (2016).
4. Fullgrabe, A. *et al.* Dynamics of Lgr6(+) Progenitor Cells in the Hair Follicle, Sebaceous Gland, and Interfollicular Epidermis. *Stem Cell Reports* **5**, 843-855 (2015).
5. Murai, K. *et al.* Epidermal Tissue Adapts to Restrain Progenitors Carrying Clonal p53 Mutations. *Cell Stem Cell* **23**, 687-699.e688 (2018).
6. Mascre, G. *et al.* Distinct contribution of stem and progenitor cells to epidermal maintenance. *Nature* **489**, 257-262 (2012).
7. Sanchez-Danes, A. *et al.* Defining the clonal dynamics leading to mouse skin tumour initiation. *Nature* **536**, 298-303 (2016).
8. Lim, X. *et al.* Interfollicular epidermal stem cells self-renew via autocrine Wnt signaling. *Science* **342**, 1226-1230 (2013).
9. Potten, C.S. The epidermal proliferative unit: the possible role of the central basal cell. *Cell Tissue Kinet* **7**, 77-88 (1974).
10. Clayton, E. *et al.* A single type of progenitor cell maintains normal epidermis. *Nature* **446**, 185-189 (2007).
11. Antal, T. & Krapivsky, P.L. Exact solution of a two-type branching process: clone size distribution in cell division kinetics. *Journal of Statistical Mechanics: Theory and Experiment* P07028 (2010).
12. Gillespie, D. Exact Stochastic Simulation of Coupled Chemical Reactions. *The Journal of Physical Chemistry* **81**, 2340-2361 (1977).
13. Gillespie, D.T. A general method for numerically simulating the stochastic evolution of coupled chemical reactions. *Journal of Computational Physics* **22**, 403-434 (1976).
14. Wilkinson, D.J. *Stochastic modelling for systems biology*". 3rd Edition. Chapman and Hall/CRC. (2018), Edn. 3rd. (Chapman and Hall/CRC., London; 2018).
15. Rompolas, P. *et al.* Spatiotemporal coordination of stem cell commitment during epidermal homeostasis. *Science* **352**, 1471-1474 (2016).
16. Hartigan, J.A. & Hartigan, P.M. The Dip Test of Unimodality. *Ann. Statist.* **13**, 70-84 (1985).
17. Silverman, B.W. Using Kernel Density Estimates to Investigate Multimodality. *Journal of the Royal Statistical Society: Series B (Methodological)* **43**, 97-99 (1981).
18. Cheng, M.-Y. & Hall, P. Calibrating the excess mass and dip tests of modality. *Journal of the Royal Statistical Society: Series B (Statistical Methodology)* **60**, 579-589 (1998).
19. Hall, P. & York, M. ON THE CALIBRATION OF SILVERMAN'S TEST FOR MULTIMODALITY. *Statistica Sinica* **11**, 515-536 (2001).
20. Fisher, N.I. & Marron, J.S. Mode testing via the excess mass estimate. *Biometrika* **88**, 499-517 (2001).
21. Ameijeiras-Alonso, J., Crujeiras, R.M. & Rodríguez-Casal, A. Mode testing, critical bandwidth and excess mass. *TEST* (2018).
22. Turner, B.M. & Van Zandt, T. A tutorial on approximate Bayesian computation. *Journal of Mathematical Psychology* **56**, 69-85 (2012).

23. Doupe, D.P., Klein, A.M., Simons, B.D. & Jones, P.H. The ordered architecture of murine ear epidermis is maintained by progenitor cells with random fate. *Dev Cell* **18**, 317-323 (2010).
24. Gomez, C. *et al.* The Interfollicular Epidermis of Adult Mouse Tail Comprises Two Distinct Cell Lineages that Are Differentially Regulated by Wnt, Edaradd, and Lrig1. *Stem Cell Reports* **1**, 19-27 (2013).